Fast ISAR Imaging based on High Frequency Scattered Fields from Quadratic Patches

An Wen Wu [1], Yu Mao Wu [1,*], Ya-Qiu Jin [1], Hongcheng Yin [2], Chonghua Fang [3], and Nan Zhang [1]

[1] Key Laboratory for Information Sciences of Electromagnetic Waves (MoE)
School of Information Science and Technology, Fudan University, Shanghai, 200433, China

[2] National Electromagnetic Scattering Laboratory, 100854, Beijing, China

[3] Science and Technology on Electromagnetic Compatibility Laboratory
China Ship Development and Design Center, Wuhan, 430064, China
awwu17@fudan.edu.cn, yumaowu@fudan.edu.cn*, yqjin@fudan.edu.cn, yinhc207@yahoo.com.cn, 27634073@qq.com, zhangnan16@fudan.edu.cn

Abstract ─ This paper implements the two-dimensional (2D) non-uniform Inverse Fast Fourier Transformation (NUFFT) to Inverse Synthetic Aperture Radar (ISAR) imaging. The complexity of two-dimensional NUFFT is $O(MN\log_2 MN)$, which is better than direct calculation with complexity $O(M^2N^2)$ and has controllable interpolation error. As for the echo scattered fields acquisition with respect to multiple frequencies and azimuth angles, we use physical optics (PO) method based on quadratic discretization to reduce the patch number to two orders of magnitude, compared with planar discretization. Three examples prove that the 2D imaging process has nearly equal accuracy and higher efficiency.

Index Terms ─ ISAR imaging, non-uniform FFT, physical optics, quadratic discretization.

I. INTRODUCTION

Inverse Synthetic Aperture Radar (ISAR) imaging is an important technique for further automatic target recognition (ATR) by acquiring high resolution two-dimensional or three-dimensional radar image with targets' detailed information like size, shape, structure and posture [1]. The Polar Format Algorithm (PFA) is one of the earliest imaging algorithms adopted for spotlight SAR and extensively applied in practical monostatic SAR systems [2]. The imaging algorithm contains two steps: 1) Store the scattered fields in polar form with respect to multiple frequencies and azimuth angles; 2) Apply two-dimensional inverse Fourier transform of the scattered data matrix after interpolating the scattered data into equally spaced grid.

In the electromagnetic (EM) scattering, when the target size is much larger than the wavelength, the EM scattered problems can be solved by high frequency methods [3,4]. Macdonald [5] proposed the physical optics (PO) approximation method to simulate high frequency electromagnetic scattered fields from large-scale radar targets. The PO method is executed based on three assumptions: 1) The target is meshed by sizeable planar or curved patches. The induced currents on every illuminated patch determined by the incident field and independent with each other. 2) Far-field approximation, the radius of curvature of the target is much larger than the incident wavelength. 3) Kirchhoff approximation for calculating the scattered fields. As for solving the surface integral of scattered fields, Ludwig [6] and Gordon [7] derived the analytical expression to calculate the PO scattered fields from the planar patch. Rius [8] proposed GRECO method considering the GPU's rendering function and converting the surface integral into a coherent addition of pixels. Conde [9] used the Stationary Phase Method (SPM) to radiation pattern of antennas. Wu and Chew [10,11] extended the steepest descent path method into calculating the PO integrals from the quadratic patches. In order to meet the second assumption, the planar patch size is nearly λ/8, while the quadratic patch size is 1λ or larger. The quadratic patch size is much larger than planar patch, the memory consumption is reduced with higher frequency. As for lit patch judging, Ling and Bhalla [12,13] proposed the shooting and bouncing ray technique (SBR), which calculates the intersections between the incident rays and surface element and compares the distance to determine the illuminated or shadowed part. To this day, the GPU's zbuffer technique is introduced to accelerate the shadowing process and applied in many electromagnetic calculation softwares.

Submitted On: April 25, 2019
Accepted On: June 17, 2019

Fast Fourier transforms (FFT) are widely used for many applications in engineering, science, and mathematics, which should be implemented on the uniform distributed data. However, the polar format [14] sampled scattered fields are non-uniform in Cartesian coordinate. Appropriate interpolation methods need to be implemented to transform the data into uniform distributed space. For interpolation on complex data, the complex values are divided into absolute and phase part, the interpolation method operates on two parts respectively. Therefore, the interpolation function requires linear phase response. Different from the traditional interpolation method which interpolates the complex form scattered fields, Dutt and Rokhlin [15] proposed non-uniform Fast Fourier Transformation (NUFFT) which interpolates the sequence of Fourier exponential function. [16-19] discussed the algorithm improvement and relative applications. Song and Liu implement the NUFFT into radar imaging [20] and radially encoded MR imaging (MRI) [21]. The NUFFT method interpolates the sequence of exponential function rather than the complex form scattered fields, which has least square error and higher efficiency.

In this work, the PO method for calculating scattered fields on quadratic patches is illustrated in Section II. The NUFFT method in ISAR imaging is described in Section III. Section IV shows the numerical results of three different targets with different shape and size.

II. THE PO SCATTERED FIELD ON QUADRATIC DISCRETIZATION PATCHES

A. The PO scattered fields

We consider a perfectly conducting (PEC) target illuminated by a time harmonic plane wave with time impedance e^{-iwt}. The PO scattered field can be derived from the Stratton-Chu formula:

$$\mathbf{E}_s(\mathbf{r}) = \frac{-ikZ_0e^{ikr}}{4\pi r}\hat{\mathbf{r}}\times\hat{\mathbf{r}}\times\int_{\partial\Omega} dS(\mathbf{r}')\mathbf{J}_{\mathrm{PO}}(\mathbf{r}')e^{-ik\hat{\mathbf{r}}\cdot\mathbf{r}'}, \quad (1)$$

where, $\partial\Omega$ is the illuminated region of the target, $\mathbf{r}'$ is the position vector of the point on the region $\partial\Omega$, $\hat{\mathbf{r}}$ and r are the unit vector and the amplitude of the scattered direction, k is the wave number, Z_0 is the wave impedance of free space. The surface induced PO current $\mathbf{J}_{\mathrm{PO}}(\mathbf{r}')$ is approximated by:

$$\mathbf{J}_{\mathrm{PO}}(\mathbf{r}') = \begin{cases} 2\hat{\mathbf{n}}(\mathbf{r}')\times\mathbf{H}^{(i)}(\mathbf{r}'), & \mathbf{r}'\in\partial\Omega \\ 0, & \mathbf{r}'\notin\partial\Omega \end{cases}, \quad (2)$$

$\hat{\mathbf{n}}(\mathbf{r}')$ is the outward unit normal vector of region $\partial\Omega$, $\mathbf{H}^{(i)}(\mathbf{r}')$ is the incident magnetic field on the target surface. The incident wave has the following form:

$$\mathbf{H}^{(i)}(\mathbf{r}') = \frac{1}{Z_0}\hat{\mathbf{r}}^{(i)}\times\mathbf{E}^{(i)}(\mathbf{r}'),\ \ \mathbf{E}^{(i)}(\mathbf{r}') = \mathbf{E}_0^{(i)}e^{ik\hat{\mathbf{r}}^{(i)}\cdot\mathbf{r}'}. \quad (3)$$

Then, we substitute equations (2), (3) into equation (1) and obtain the general scattered fields calculation formula:

$$\mathbf{E}_s(\mathbf{r}) \approx \int_S dS(\mathbf{r}')g(\mathbf{r}')e^{ikf(\mathbf{r}')}, \quad (4)$$

with the phase function $f(\mathbf{r}')$ and amplitude function $g(\mathbf{r}')$ that,

$$g(\mathbf{r}') = \frac{-ike^{ikr}}{2\pi r}\hat{\mathbf{r}}\times\hat{\mathbf{r}}\times\left(\hat{\mathrm{n}}(\mathbf{r}')\times\hat{\mathbf{r}}^{(i)}\times\mathbf{E}_0^{(i)}\right), \quad (5)$$

$$f(\mathbf{r}') = \left(\hat{\mathbf{r}}^{(i)}-\hat{\mathbf{r}}\right)\cdot\mathbf{r}'. \quad (6)$$

B. The quadratic discretization

For solving the integral equation (4) on quadratic patches, we have to apply affine transformation to transform every arbitrary quadratic patch into a standard square patch with parameters (ξ,η). For standard square patch, the interpolation formula for a quadratic patch:

$$\mathbf{r}'(\xi,\eta) = \sum_{j=1}^{8} N_j(\xi,\eta)\mathbf{r}_j, \quad (7)$$

$\mathbf{r}_j$ is the three-dimensional coordinates of the critical points of quadratic patch with respect to coordinate $(\mathrm{x},\mathrm{y},\mathrm{z})$ and $\mathbf{r}'(\xi,\eta)$ is the three dimensional coordinates with respect to parameter (ξ,η).

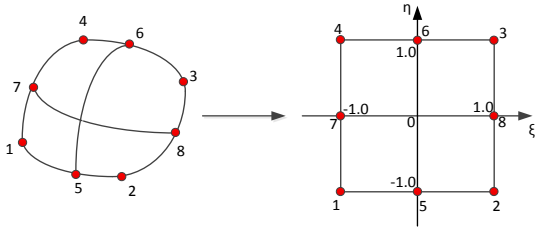

Fig. 1. The affine transformation from an arbitrary patch into a standard square patch with 8 nodes.

The standard square patch is shown in Fig. 1 above. For nodes in different place, the shape function $N_j(\xi,\eta)$ are different. For the four vertexes (j=1,2,3,4), the shape function is:

$$N_j(\xi,\eta) = \frac{1}{4}\left(1+\xi_j\xi\right)\left(1+\eta_j\eta\right)\left(\xi_j\xi+\eta_j\eta-1\right), \quad (8)$$

for the middle nodes on the edge where $\xi_j = 0$ (j=5,6), the shape function is:

$$N_j(\xi,\eta) = \frac{1}{2}\left(1-\xi^2\right)\left(1+\eta_j\eta\right), \quad (9)$$

for the middle nodes on the edge where $\eta_j = 0$ (j=7,8), the shape function is:

$$N_j(\xi,\eta) = \frac{1}{2}\left(1-\eta^2\right)\left(1+\xi_j\xi\right). \quad (10)$$

We substitute equations (7-10) to equation (4), the scattered field expression of a quadratic patch is:

$$\mathbf{E}_s(\mathbf{r}) \approx \sum_{n=1}^{N}\int_{-1}^{1}\int_{-1}^{1} g_n\left(\mathbf{r}'(\xi,\eta)\right)e^{ikf_n\left(\mathbf{r}'(\xi,\eta)\right)}D_e d\xi d\eta, \quad (11)$$

with integral infinitesimal $D_e = \left|\mathbf{r}'_{\xi}(\xi,\eta) \times \mathbf{r}'_{\eta}(\xi,\eta)\right|$. $\mathbf{r}'_{\xi}(\xi,\eta) = \frac{\partial \mathbf{r}'(\xi,\eta)}{\partial \xi}$ and $\mathbf{r}'_{\eta}(\xi,\eta) = \frac{\partial \mathbf{r}'(\xi,\eta)}{\partial \eta}$ are the partial derivative of ξ and η.

For approximating the integral which has fixed integral domain [-1,1] ×[-1,1], we use the Lagrange interpolation polynomials to approximate the integral into closed-form formulation:

$$\mathbf{E}_s(\mathbf{r}) \approx \sum_{n=1}^{N} \int_{-1}^{1}\int_{-1}^{1} \boldsymbol{G}_n(\xi,\eta) e^{ikF_n(\xi,\eta)} d\xi d\eta, \quad (12)$$

where the function $\boldsymbol{G}_n(\xi,\eta)$ and $F_n(\xi,\eta)$ have the polynomials form on *n-th* patch as:

$$F_n(\xi,\eta) = F_0 + F_1\xi + F_2\xi^2 + F_3\eta + F_4\eta^2$$
$$\boldsymbol{G}_n(\xi,\eta) = \boldsymbol{G}_0 + \boldsymbol{G}_1\xi + \boldsymbol{G}_2\xi^2 + \boldsymbol{G}_3\eta + \boldsymbol{G}_4\eta^2. \quad (13)$$

We choose 5 points $\mathbf{r}_1, \mathbf{r}_5, \mathbf{r}_2, \mathbf{r}_8, \mathbf{r}_3$ and substitute the coordinates to equation (13) to calculate the coefficients $(F_0, F_1, F_2, F_3, F_4)$ and $(\boldsymbol{G_0}, \boldsymbol{G_1}, \boldsymbol{G_2}, \boldsymbol{G_3}, \boldsymbol{G_4})$.

C. The stationary phase method

The Stationary Phase Method (SPM) [22-24] is applied to solve the double integrals. From the geometrical theory of diffraction, when the target size is much larger than the incident wavelength, the radar scattered fields of the target is equivalent to the superposition of multiple scattering centers. Similar to the GTD model [25], the scattered field of quadric patch can be approximated by the sum of critical points: stationary phase points (points that satisfy equation (14) below and showed in Fig. 2 in detail), boundary points ($\mathbf{r}_5, \mathbf{r}_6, \mathbf{r}_7, \mathbf{r}_8$ from Fig. 1 and shown in detail in Fig. 3) and vertex points ($\mathbf{r}_1, \mathbf{r}_2, \mathbf{r}_3, \mathbf{r}_4$ from Fig. 1 and shown in detail in Fig. 4).

$$\hat{\mathbf{r}} \cdot \mathbf{r}'_{\xi}(\xi,\eta) = 0 \text{ and } \hat{\mathbf{r}} \cdot \mathbf{r}'_{\eta}(\xi,\eta) = 0. \quad (14)$$

The contributions of the stationary phase point $\boldsymbol{s}(\xi_s,\eta_s)$ is:

$$\boldsymbol{I_s} = \frac{\pi \boldsymbol{G}^s}{k} e^{-ikF^s} \sqrt{\frac{1}{\left|F^s_{\xi\xi}F^s_{\eta\eta} - \left(F^s_{\xi\eta}\right)^2\right|}} e^{-ik\frac{\pi}{4}\sigma(\delta+1)}, \quad (15)$$

where $\boldsymbol{G}^s = \boldsymbol{G}(\xi_s,\eta_s)$ and $F^s = F(\xi_s,\eta_s)$. $F_{\xi\xi}, F_{\eta\eta}, F_{\xi\eta}$ are the second parametric derivatives of $F(\xi,\eta)$. $\sigma = \text{sign}(F_{\eta\eta})$ and $\delta = \text{sign}(F_{\xi\xi}F_{\eta\eta} - (F_{\xi\eta})^2)$.

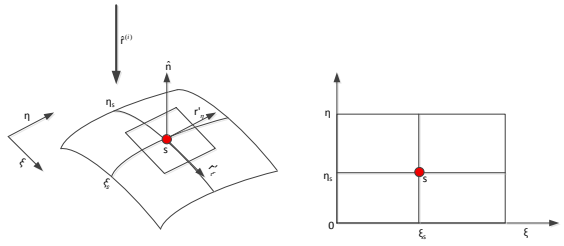

Fig. 2. Stationary phase point $\boldsymbol{s}(\xi_s,\eta_s)$ on a quadratic patch.

The contributions of the boundary point $\boldsymbol{c}(\xi_c,\eta_c)$ is:

$$\boldsymbol{I_c} = -i(-1)^{\alpha} \frac{\boldsymbol{G}^c}{k} e^{-ikF^c} \frac{1}{F^c_{\alpha}} \sqrt{\frac{2i\pi}{kF^c_{\beta\beta}}}, \quad (16)$$

where $\alpha \equiv \xi, \beta \equiv \eta$ at the boundaries $\xi = 0$ and $\xi = 1$, and $\alpha \equiv \eta, \beta \equiv \xi$ at the boundaries $\eta = 0$ and $\eta = 1$.

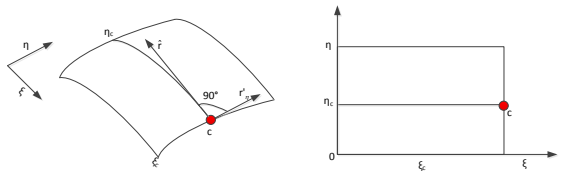

Fig. 3. Boundary point $\boldsymbol{c}(\xi_c,\eta_c)$ on a quadratic patch.

The contributions of the vertex point $\boldsymbol{v}(\xi_v,\eta_v)$ is:

$$\boldsymbol{I_v} = -\boldsymbol{G}^v e^{-ikF^v} \frac{(-1)^{\xi_v+\eta_v}}{k^2 F^v_{\xi} F^v_{\eta}}, \quad (17)$$

where $\boldsymbol{G}^v = \boldsymbol{G}(\xi_v,\eta_v)$ and $F^v = F(\xi_v,\eta_v)$. F_{ξ} and F_{η} are the parametric derivatives of $F(\xi,\eta)$.

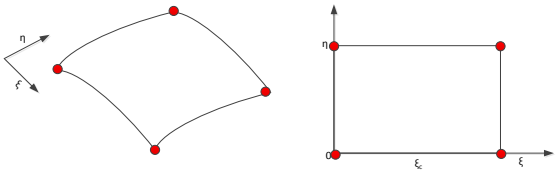

Fig. 4. Vertex point $\boldsymbol{v}(\xi_v,\eta_v)$ on a quadratic patch.

Considering all the critical points' contribution, the scattered field can be written as:

$$\mathbf{E}_s(\mathbf{r}) \approx \sum_{n=1}^{N} \boldsymbol{I^n_s} + \boldsymbol{I^n_c} + \boldsymbol{I^n_v}. \quad (18)$$

PO method calculates the scattered field of the illuminated area of the target. For lit-judging, Rius [26] used GPU's zbuffer storage to simplify the lit-judgement of the target. Fan and Guo [27] implemented the fast patch-lit-judge method in hybrid EM method with the efficient open graphics library (OpenGL).

III. NON-UNIFORMED FFT (NUFFT) IMAGING ALGORITHM

The ISAR image can be calculated by [28]:

$$I(\hat{x},\hat{y}) = \frac{1}{(2\pi)^2} \iint \mathrm{S}(f,\theta)\, e^{j2\pi K_x(f,\theta)\hat{x} + j2\pi K_y(f,\theta)\hat{y}} df d\theta, \quad (19)$$

where $\mathrm{S}(f,\theta)$ is the scattered field with respect to the different incident frequency f and azimuth angle θ, $\hat{x}$ and $\hat{y}$ are the pixel index in image domain. $K_x = \frac{2\cos\theta}{\lambda}$ and $K_y = \frac{2\sin\theta}{\lambda}$, the target reconstruction function is the 2D-IFFT with respect to K_x and K_y. The sample number of frequency f is M and azimuth angle θ is N, the

complexity of 2D-IFFT is $O(MNlog_2MN)$.

Discretize equation (19) and we form equation (20), which can be used to calculate the value of every pixel of the image. For solving the summation, the complexity is $O(M^2N^2)$:

$$I(\hat{x},\hat{y}) = \frac{1}{(2\pi)^2}\sum_{f_{min}}^{f_{max}}\sum_{\theta_{min}}^{\theta_{max}} \mathrm{S}(f,\theta)e^{j2\pi K_x(f,\theta)\hat{x}+j2\pi K_y(f,\theta)\hat{y}}. \quad (20)$$

As shown in Fig. 5 below, the sampled scattered fields are uniform on frequency−azimuth angle $k-\theta$ domain (blue points) and non-uniform on K_x-K_y domain (red points).

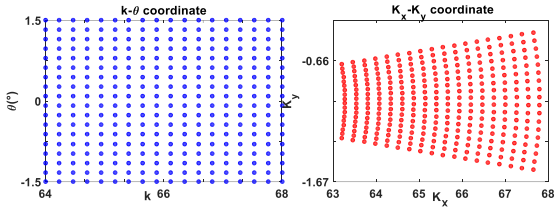

(a) (b)

Fig. 5. The sampled scattered fields distribution: (a) non-uniform distributed in K_x-K_y domain, and (b) uniform distributed in $k-\theta$ domain. We take 18 sampling points for k and θ, respectively.

Different from traditional interpolation algorithms, NUFFT method interpolates the sequence of exponential function rather than the sampled scattered fields matrix. Two-dimensional NUFFT equals to two one-dimensional NUFFT implemented in two dimensions [29,30], that is, 2D-NUFFT is the tensor product of two one-dimensional NUFFT. We just need to consider the one-dimensional Inverse Discrete Fourier Transform:

$$X_n = \frac{1}{N}\sum_{k=1}^{N} x(k)e^{j\frac{2\pi}{N}n\omega_k}, \quad (21)$$

where $\omega_k \in \left[-\frac{N}{2},\frac{N}{2}-1\right]$, $k=1,2,\dots,N$, $n=-\frac{N}{2},-\frac{N}{2}+1,\dots,\frac{N}{2}-1$. Consider the equations that every exponential function $e^{j\frac{2\pi}{N}n\omega_k}$ can be written as the sum of the nearest (2Q+1) terms uniformly-spaced Fourier series:

$$s_n e^{j\frac{2\pi}{N}n\omega_k} \approx \sum_{k=[G\omega_k]-Q}^{k=[G\omega_k]+Q} x_k(\omega_k)e^{j\frac{2\pi}{GN}nk}, \quad (22)$$

where G is the oversampling factor and (2Q+1) is the length of interpolation kernel. $s_n>0$ is chosen to minimize the approximation error. For this work, we choose $s_n=\cos\frac{\pi n}{GN}$. [] is the rounding operation. We substitute $n=-\frac{N}{2},-\frac{N}{2}+1,\dots,\frac{N}{2}-1$ and write the equation as equation (23).

Equation (23) is an overdetermined equation set of N linear equations with (2Q+1) unknowns and (2Q+1)$\ll N$. We use the least square solution as the approximation of the solution of the overdetermined equation set. We write the equation set in simplified form:

$$B = Ax, \quad (24)$$

and the least-square solution x^* is:

$$x^* = x_k(\omega_k) = \begin{bmatrix} x_{[G\omega_k]-Q}(\omega_k) \\ x_{[G\omega_k]-Q+1}(\omega_k) \\ \vdots \\ x_{[G\omega_k]+Q}(\omega_k) \end{bmatrix} = \left(A^\dagger A\right)^{-1}A^\dagger B, \quad (25)$$

where $A^\dagger$ denotes the complex-conjugate transpose of matrix A. Substitute $x_k(\omega_k)$ into equation (21) and transform the non-uniform data into uniform space, as equation (26) illustrates below:

$$\begin{bmatrix} (s_{-\frac{N}{2}})e^{j\frac{2\pi}{N}\omega_k(-\frac{N}{2})} \\ (s_{-\frac{N}{2}+1})e^{j\frac{2\pi}{N}\omega_k(-\frac{N}{2}+1)} \\ \vdots \\ (s_{\frac{N}{2}-1})e^{j\frac{2\pi}{N}\omega_k(\frac{N}{2}-1)} \end{bmatrix} = \begin{bmatrix} e^{j\frac{2\pi}{GN}(-\frac{N}{2})([G\omega_k]-Q)} & e^{j\frac{2\pi}{GN}(-\frac{N}{2})([G\omega_k]-Q+1)} & \cdots & e^{j\frac{2\pi}{GN}(-\frac{N}{2})([G\omega_k]+Q)} \\ & e^{j\frac{2\pi}{GN}(-\frac{N}{2}+1)([G\omega_k]-Q)} & \ddots & \ddots & \vdots \\ & \vdots & \ddots & \ddots & \vdots \\ & e^{j\frac{2\pi}{GN}(\frac{N}{2}-1)([G\omega_k]-Q)} & \cdots & \cdots & e^{j\frac{2\pi}{GN}(\frac{N}{2}-1)([G\omega_k]+Q)} \end{bmatrix} \cdot \begin{bmatrix} x_{[G\omega_k]-Q}(\omega_k) \\ x_{[G\omega_k]-Q+1}(\omega_k) \\ \vdots \\ x_{[G\omega_k]+Q}(\omega_k) \end{bmatrix}. \quad (23)$$

Then, IFFT can be implemented on equally-spaced $x'(k)$. For 2D ISAR imaging, operate one-dimensional IFFT on range and cross range direction respectively.

For actual measurement, the incident signal is considered as step-frequency signal, pulse signal with a fixed frequency step. The amplitude and initial phase of each sample point are consistent.

$$\begin{aligned} X_n &= \frac{1}{N}\sum_{k=1}^{N} x(k)e^{j\frac{2\pi}{N}n\omega_k} \\ &= \frac{1}{Ns_n}\sum_{k=1}^{N} x(k)\left(\sum_{q=-Q}^{Q} x_{q+[G\omega_k]}(\omega_k)e^{j\frac{2\pi}{GN}n(q+[G\omega_k])}\right) \\ &= \frac{1}{Ns_n}\sum_{k=-\frac{GN}{2}}^{\frac{GN}{2}-1} x'(k)e^{j\frac{2\pi}{GN}nk}. \end{aligned} \quad (26)$$

As for the resolution, the range resolution δ_r is related to the bandwidth of the incident wideband signal, the cross range resolution δ_{cr} is related to azimuth range scan:

$$\delta_r = \frac{c}{2B}, \delta_{cr} = \frac{\lambda_c}{2\sin\Delta\varphi}, \quad (27)$$

where c is light speed in vacuum, B is the bandwidth of the incident wideband signal, λ_c is the center wavelength corresponding to center frequency f_c, $\Delta\varphi$ is the angular scan. The resolution denotes the actual distance represented by every pixel in image.

III. NUMERICAL RESULTS

We bring three targets with different size and shape to discussion, two perfect electric conductor (PEC) spheres with different radius, a glider most consisting of curved surfaces, a finely modeled ship with lots of flat surfaces. Under spherical coordinate system, θ (elevation angle) is the angle between the scattered direction and $+\hat{\mathbf{z}}$ axis. φ (azimuth angle) is the angle between the projection of the scattered direction in the xOy plane and the $+\hat{\mathbf{x}}$ axis. The scattering pattern is monostatic and incident electric field $\mathbf{E}_0^{(i)}$ polarizes along $\hat{\boldsymbol{e}}_{\boldsymbol{\theta}}$ direction.

In order to meet the Far-field approximation, the radius of curvature of the target is much larger than the incident wavelength, the planar patch size is nearly $\lambda/8$, while the quadratic patch size is 1λ or larger. We use *Altair HyperMesh 14.0* software to discretize the geometry at "second order" and "quads only" mode. Table 1 shows the patch number using planar discretization and quadratic discretization respectively. Quadratic discretization reduces the patch number to two orders of magnitude. Table 2 shows the information of the incidence and the size of three different targets.

Table 1: The numbers and sizes of patches by using the quadratic discretization and plane discretization for the different targets

Targets	**Planar Patch (λ/8)**	**Quadratic Patch (1λ)**
Two spheres	365432	5748
Glider	8901418	100389
Ship	39144518	120929

Table 2: The parameters of the incident wave and the size of three targets

Target 1: Two spheres	Radius: 0.5m 1m Center distance: 10m Patch number: 5748
Target 2: A glider	Size: 14m×14m×2m Patch number: 100389
Target 3: A ship	Size: 30m×3.5m×4.6m Patch number: 120929
Frequency center (f_c)	10GHz
θ	60°
φ	43.5°~46.5°
Bandwidth (B)	600MHz
Angular scan (Δφ)	3°
Frequency samples	128
φ samples	128
Range resolution	$\frac{c}{2B}$ =0.25m
Azimuth resolution	$\frac{\lambda}{2sin\Delta\varphi}$ =0.29m

As for the accuracy comparison, we choose the image formed by NUFFT equation (19) and by directly calculating the double integral in equation (20). For estimating the performance of the NUFFT method, we introduce the relative L_2 error to discuss:

$$e_2 = avg\left(\frac{\|\hat{I}-I\|_2^2}{\|I\|_2^2}\right), \tag{28}$$

where I is the image of direct calculation and $\hat{I}$ is the image generated by NUFFT. We calculate the average error of every pixel. The results are showed in Table 3 at the end of this chapter.

A. Two PEC sphere

Firstly, we take two PEC spheres with different radius as example. The geometry and the quadratic discretization are shown in Fig. 6. The detailed parameters are illustrated in Table 2.

Fig. 6. The geometry and the quadratic discretization of two different size spheres.

From Fig. 7 below, the 2D image generated by NUFFT and direct calculation agree well. The image tells that center sphere has smaller radius and lower amplitude. From Fig. 8, the range profile shows agreement and the two spheres can be well distinguished.

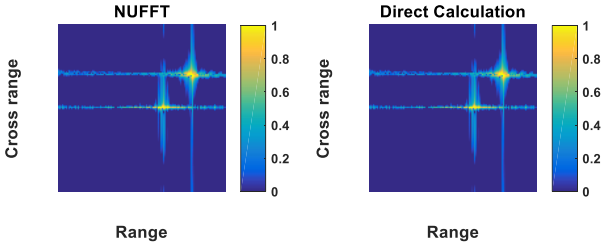

(a) (b)

Fig. 7. The comparison between: (a) NUFFT and (b) direct calculation of ISAR imaging of two PEC spheres.

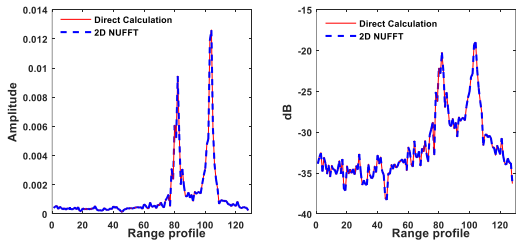

(a) (b)

Fig. 8. The range profile: (a) amplitude and (b) dBsm comparison between NUFFT and direct calculation of ISAR imaging of two PEC spheres.

B. A glider

The glider geometry and quadratic discretization are showed in Fig. 9. The geometry mostly consists of curved surface and simple struction like the streamline airframe and light wings to reduce the air friction. The comparison between NUFFT and direct calculation is illustrated in Fig. 10.

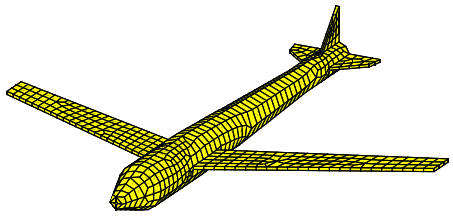

Fig. 9. The quadratic discretization of a glider.

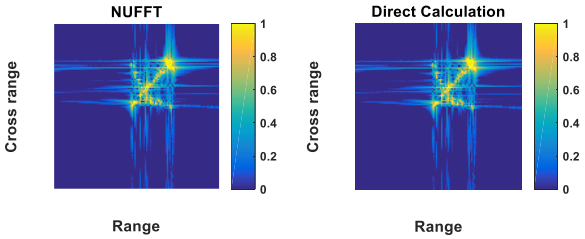

Fig. 10. The comparison between: (a) NUFFT and (b) direct calculation of ISAR imaging of a glider.

From Fig. 10, the 2D image of NUFFT and direct calculation of the glider agree very well. The image tells the detailed structure of the glider. The shape is well represented and the empennage has relatively obvious contribution. Figure 11 further verifies the scattered characteristic of the glider from range profile.

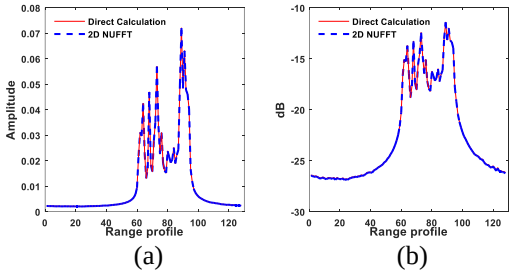

Fig. 11. The range profile: (a) amplitude and (b) dBsm comparison between NUFFT and direct calculation of ISAR imaging of a glider.

C. A ship

We take a finely modeling ship as the third example. As Fig. 12 shows, the ship is mostly composed of plane elements like the deck and control rooms in the ship. When the ship is discretized into quadratic patches, some are quite close to planar patches. We choose the same incident plane wave for test.

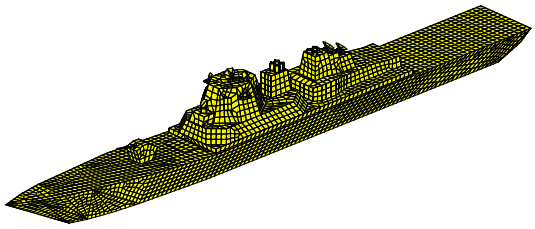

Fig. 12. The geometry and the quadratic discretization of a finely modeling ship.

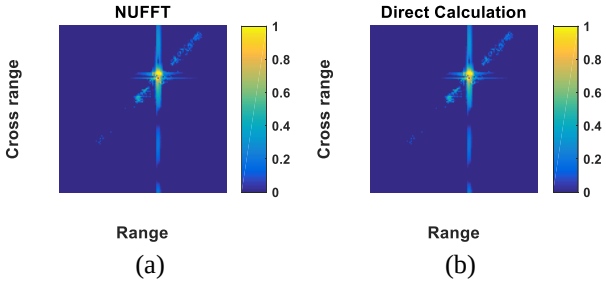

Fig. 13. The comparison between: (a) NUFFT and (b) direct calculation of ISAR imaging of a finely modeled ship.

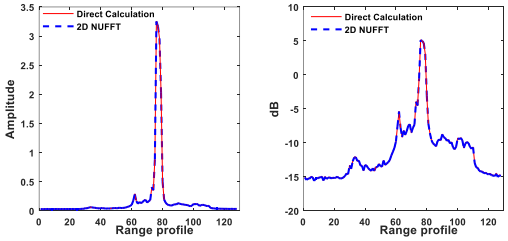

Fig. 14. The range profile: (a) amplitude (b) dBsm comparison between NUFFT and direct calculation of ISAR imaging of a finely modeled ship.

From Fig. 13, the 2D image of NUFFT and direct calculation of the ship agree well. From the ISAR image and the range profile in Fig. 14, we can tell that the middle part of the ship has the strongest contribution to the image compared with other parts. However, the structure of the ship is not very clear. The reason possibly is that the basic component of the finely modeling ship is flat, like deck and hull. The quadratic discretization generates error. We may conclude that for targets consisting of large flat surfaces, we need to choose quadratic patches combined with planar patches to finely describe the target.

The relative L_2 error shows in Table 3 below. We can tell from it that the relative L_2 error is overall quite small and increases very slowly as the increase of the interpolation kernel size Q. It indicates that the NUFFT method generates minor error, which is introduced by solving the overdetermined equations utilizing the least square solution.

Table 3: The relative L_2 error defined in equation (27) on different size of interpolation kernel determined by Q

Targets G**=2**	Q**=2**	Q**=4**	Q**=8**	Q**=16**
Two spheres	0.77%	1.09%	1.26%	1.34%
Glider	0.23%	0.43%	0.61%	0.73%
Ship	0.12%	0.19%	0.25%	0.30%

The time comparison shows in Table 4 below. NUFFT method reduces the time consumption a lot. The time consumption contains obtaining the interpolation coefficients by solving the overdetermined equations, so that the theoretical time comparison from the complexity is not fully achieved. As for the memory consumption, NUFFT has less memory usage. The CPU is Intel(R) Core (TM) i7-4790 at 3.6GHz, the simulation software is Matlab R2015b.

Table 4: The time consuming comparison between direct calculation and NUFFT on G=2, Q=4; in order to make difference more obvious, we choose the total time and memory consumption of 100 tests

	Direct Calculation	**NUFFT**
Time (second)	30.214s	14.646s
Memory (kilobyte)	296kB	212kB

IV. CONCLUSION

This work implements the two-dimensional non-uniform Inverse Fast Fourier Transformation to Inverse Synthetic Aperture Radar imaging. The complexity of two-dimensional NUFFT is $O(MN\log_2 MN)$, compared with direct computation with complexity $O(M^2N^2)$, has higher computational efficiency and nearly equal imaging accuracy. The error is controllable, generated by least squares method solving overdetermined equations. The physical optics (PO) method based on quadratic discretization reduces the patch number to one hundredth, compared with planar discretization. In general, the work achieves fast simulation for ISAR imaging on complex targets, providing basis for further automatic radar recognition (ATR).

ACKNOWLEDGMENT

This work is supported in part by National Key R&D Program of China No. 2017YFB0502703, National Natural Science Foundation of China under Grant No. 11571196, Open Research Fund of State Key Laboratory of Pulsed Power Laser Technology, Electronic Engineering Institute, State Key Laboratory of Applied Optics, Changchun Institute of Optics, Fine Mechanics and Physics.

REFERENCES

[1] Mensa, L. Dean, *High Resolution Radar Imaging*. Artech House, 1981.

[2] J. L. Walker, "Range-doppler imaging of rotating objects," *IEEE Transactions on Aerospace and Electronic Systems.*, vol. 16, no. 1, pp. 23-52, Jan. 1980.

[3] J. A. Kong, *Electromagnetic Wave Theory*. New York, NY, USA: Wiley-Interscience, 1990.

[4] Y. Q. Jin, *Electromagnetic Scattered Modelling for Quantitative Remote Sensing*. Singapore: World Science Press, 2000.

[5] H. M. Macdonald, "The effect produced by an obstacle on a train of electric waves," *Philosophical Transactions of the Royal Society of London*, vol. 212, pp. 299-337, 1913.

[6] A. C. Ludwig, "Computation of radiation patterns involving numerical double integration," *IEEE Trans. Antennas Propag*., vol. 16, no. 6, pp. 767-769, 1968.

[7] W. B. Gordon, "Far-field approximations to the Kirchhoff-Helmholtz representation of scattered fields," *IEEE Trans. Antennas Propagat.*, vol. 23, no. 7, pp. 590-592, July 1975.

[8] J. M. Rius, M. Ferrando, and L. Jofre, "High-frequency RCS of complex radar targets in real-time." *IEEE Trans. Antennas Propagat.*, vol. 41, no. 9, pp. 1308-1319, 1993.

[9] O. M. Conde, J. Perez, and M. P. Catedra, "Stationary phase method application for the analysis of radiation of complex 3-D conducting structures," *IEEE Trans. Antennas Propagat.*, vol. 49, no. 5, pp. 724-731, 2001.

[10] Y. M. Wu and W. C. Chew, "The modern high frequency methods for solving electromagnetic scattering problems," *Progr. Electromagn. Res. PIER*, vol. 156, pp. 63-82, 2016.

[11] Y. M. Wu, L. J. Jiang, and W. C. Chew, "An efficient method for computing highly oscillatory physical optics integral," *Progr. Electromagn. Res. PIER*, vol. 127, pp. 211-257, Apr. 2012.

[12] H. Ling, R.-C. Chou, and S.-W. Lee, "Shooting and bouncing rays: calculating the RCS of an arbitrarily shaped cavity," *IEEE Trans. Antennas Propagat.*, vol. 37, no. 2, pp. 194-205, Feb. 1989.

[13] R. Bhalla and H. Ling, "Image domain ray tube integration formula for the shooting and bouncing ray technique," *Radio Science*, vol. 30, no. 5, pp. 1435-1446, 1995.

[14] J. Sun, S. Mao, G. Wang, and W. Wange, "Polar format algorithm for spotlight bistatic SAR with

arbitrary geometry configuration," *Progress In Electromagnetics Research*, vol. 103, pp. 323-338, 2010.

[15] A. Dutt and V. Rokhlin, "Fast Fourier transforms for non equispaced data," *SIAM J. Sci. Comp.*, vol. 14, pp. 1368-1393, 1993.

[16] N. Nguyen and Q. H. Liu, "The regular Fourier matrices and nonuniform fast Fourier transforms," *SIAM J. Sci. Comp.*, vol. 21, no. 1, pp. 283-293, 1999.

[17] K. Natroshvili, O. Loffeld, H. Nies, A. M. Ortiz, and S. Knedlik, "Focusing of general bistatic SAR configuration data with 2-D inverse scaled FFT," *IEEE Trans. Geosci. Remote Sens.*, vol. 44, no. 10, pp. 2718-2727, Oct. 2006.

[18] Q. Liu and N. Nguyen, "An accurate algorithm for nonuniform fast fourier transform (NUFFT's)," *IEEE Microwave and Guided Wave Letters*, vol. 8, no. 1, pp. 18-20, Jan. 1998.

[19] J. A. Fessler and B. P. Sutton, "Nonuniform fast Fourier transforms using min-max interpolation," *IEEE Transactions on Signal Processing*, vol. 51, no. 2, pp. 560-574, Feb. 2003.

[20] J. Y. Song, Q. H. Liu, K. Kim, and W. R. Scott, "High-resolution 3-D radar imaging through nonuniform fast Fourier transform (NUFFT)," *Communications in Computational Physics*, vol. 1, no. 1, pp. 176-191, 2006.

[21] J. Y. Song, Q. H. Liu, S. L. Gewalt, G. Cofer, and G. A. Johnson, "Least square NUFFT methods applied to 2D and 3D radially encoded MR image reconstruction," *IEEE Transactions on Biomedical Engineering*, vol. 56, no.4, pp. 1134-1142, 2009.

[22] Y. M. Wu, L. J. Jiang, and W. C. Chew, "Computing highly oscillatory physical optics integral on the polygonal domain by an efficient numerical steepest descent path method," *Journal of Computational Physics*, vol. 236, no. 1, pp. 408-425, 2013.

[23] J. Zhang, W. M. Yu, X. Y. Zhou, and T. J. Cui, "Efficient evaluation of the physical-optics integrals for conducting surfaces using the uniform stationary phase method," *IEEE Trans. Antennas Propagat.*, vol. 60, no. 5, pp. 2398-2408, May 2012.

[24] F. S. de Adana, O. Gutierrez, I. Gonzalez, M. F. Catedra, and L. Lozano, *Practical Applications of Asymptotic Techniques in Electromagnetics*. Norwood, MA, 2011.

[25] L. C. Potter, Da-Ming Chiang, R. Carriere, and M. J. Gerry, "A GTD-based parametric model for radar scattering," *IEEE Trans. Antennas Propagat.*, vol. 43, no. 10, pp. 1058-1067, 1995

[26] J. M. Rius, A. Carbo, J. Bjerkemo, et al., "New graphical processing technique for fast shadowing computation in PO surface integral," *IEEE Trans. Antennas Propagat.*, vol. 62, no. 5, pp. 2587-2595, 2014.

[27] T. Q. Fan, L. X. Guo, and W. Liu, "A novel openGL-based MoM/SBR hybrid method for radiation pattern analysis of an antenna above an electrically large complicated platform," *IEEE Trans. Antennas Propagat.*, vol. 64, no. 1, pp. 201-209, 2016.

[28] C. Y. Dai and X. L. Zhang, "Bistatic polar format algorithm based on NUFFT method," *Journal of Electromagnetic Waves & Applications*, vol. 25, no. 17-18, pp. 2328-2340, 2011.

[29] R. Bhalla and H. Ling, "Three-dimensional scattering center extraction using the shooting and bouncing ray technique," *IEEE Trans. Antennas Propagat.*, vol. 44, no. 11, pp. 1445-1453, 1996.

[30] X. Y. He, X. Y. Zhou, and T. J. Cui, "Fast 3D-ISAR image simulation of targets at arbitrary aspect angles through nonuniform fast Fourier transform (NUFFT)," *IEEE Trans. Antennas Propagat.*, vol. 60, no. 5, pp. 2579-2602, 2012.